

Article

“Kill Two Birds with One Stone”: Urban Tree Species Classification Using Bi-Temporal Pléiades Images to Study Nesting Preferences of an Invasive Bird

Marine Le Louarn ^{1,2,*} , Philippe Clergeau ², Elodie Briche ¹ and Magali Deschamps-Cottin ¹

¹ Aix Marseille Univ, IRD, LPED, Marseille, France; elodie.briche@univ-amu.fr (E.B.); magali.deschamps-cottin@univ-amu.fr (M.D.-C.)

² Muséum National d’Histoire Naturelle, UMR CESCO, 43 rue Buffon, CP135, 75005 Paris, France; clergeau@mnhn.fr

* Correspondence: marine.le-louarn@univ-amu.fr; Tel.: +33-631-351-962

Received: 19 June 2017; Accepted: 1 September 2017; Published: 1 September 2017

Abstract: This study presents the results of object-based classifications assessing the potential of bi-temporal Pléiades images for mapping broadleaf and coniferous tree species potentially used by the ring-necked parakeet *Psittacula krameri* for nesting in the urban area of Marseille, France. The first classification was performed based solely on a summer Pléiades image (acquired on 28 July 2015) and the second classification based on bi-temporal Pléiades images (a spring image acquired on 24 March 2016 and the summer image). An ensemble of spectral and textural features was extracted from both images and two machine-learning classifiers were used, Random Forest (RF) and Support Vector Machine (SVM). Regardless of the classifiers, model results suggest that classification based on bi-temporal Pléiades images produces more satisfying results, with an overall accuracy 11.5–13.9% higher than classification using the single-date image. Textural and spectral features extracted from the blue and the NIR bands were consistently ranked among the most important features. Regardless of the classification scheme, RF slightly outperforms SVM. RF classification using bi-temporal Pléiades images allows identifying 98.5% of the tree species used by the ring-necked parakeet for nesting, highlighting the promising value of remote sensing techniques to assess the ecological requirements of fauna in urban areas.

Keywords: urban trees; Pléiades; random forest; support vector machine; object-based classification; *Psittacula krameri*

1. Introduction

Biological invasions are considered as one of the main cause of biodiversity loss, and invasive species can cause ecological and socio-economic impacts in their introduced range [1,2]. Urban areas face high-intensity risk given that several animal species kept as attractions in urban parks and zoos or as pets accidentally escaped from captivity or have been deliberately released in the wild. Most of them failed to survive and maintain a sustainable population [3,4], probably because of the low number of introduced individuals and/or an unsuitable climate. Those who are able to survive and spread may become invasive, disrupt ecosystem functioning, and negatively affect native organisms.

Examples of introduced animals that have successfully established self-sustaining populations in their introduced range include the ring-necked parakeet *Psittacula krameri*. This green parakeet is native to India and sub-Saharan Africa [5] and, due to its popularity as a pet bird, has been widely introduced in Europe through the exotic pet trade. The number of “rewilded” individuals is estimated to more than 85,000 in 2015, with increasing populations established in cities across ten European countries [6]. In its introduced range, this parakeet may cause several impacts on native biodiversity and anthropic activities. Due to its aggressive behavior, the presence of the ring-necked parakeet

prevents the access of native birds to food resources [7–9]. Breeding earlier than most of the native cavity-nesting species, the ring-necked parakeet may reduce the availability of this crucial resource to native birds such as the nuthatch *Sitta europaea* [10]. Indeed, tree cavities are considered as a limiting factor for cavity-nesting birds [11], especially in urban environments where large old trees may be more scarce than in forested areas. The ring-necked parakeet is considered a major crop pest in its native range and, in areas where it has been introduced, causes damage to agricultural areas [12]. The exponential demographic growth has raised concerns by urban planners regarding the potential negative impacts of the ring-necked parakeet and a better knowledge of the ecological requirements and the potential future distribution of this species is thus needed.

Species occurrences have become increasingly available from online databases covering a range of spatial and temporal scales. These existing databases provide new opportunities to study the relationship between successful introduced species and their environment and are widely used to predict their potential future distribution [13]. However, the information contained in these databases is often limited to the location and sometimes to the activity of species (e.g., nesting, feeding). In the case of the ring-necked parakeet which may compete with native fauna for tree cavities, useful information to acquire is its potential nesting preferences regarding the tree species in which parakeets are nesting. Traditional methods involve field investigation and random sampling of breeding bird populations to record a subset of tree species used, which is time and labor consuming and may not be representative of birds nesting preferences. An alternative method is to use available tree occurrences datasets, which may be incomplete, especially at the local scale and in private areas such as private gardens and residential areas.

Remote sensing, especially using Very High Resolution (VHR) satellite imagery, provides a time-effective and cost-efficient way to highlight new information from tree species occurrence databases by allowing one to identify tree species used by birds for nesting. Tree species mapping can be challenging in urban areas compared to more natural sites. Urban vegetation is characterized by a high diversity of trees, including exotic species with sometimes few individuals which lead to a small number of reference samples, and by some highly spatially dispersed tree individuals. Spectral characteristics of urban trees are affected by the spatial proximity of non-tree urban objects, such as buildings, which cast shadows and cause the complete or partial loss of trees spectral information [14]. Trees from the same broadleaf species may also have a different phenology due to the Urban Heat Island effect and may exhibit variability of phenological stages through the intra-urban gradient [15]. The closeness of spectral signatures among tree species can also make them difficult to discriminate. Thus, in urban areas, and in a more general way, single-date imagery may not suffice for urban tree species classification. Li et al. [16] explored the identification of five urban tree species based on object-based classification using single-date and bi-temporal WorldView-2 and WorldView-3 images. The overall accuracy increased to more than 11% when using bi-temporal images. Tigges et al. [17] reached the same conclusion and found an overall accuracy of 85.5% when using multi-temporal images for the classification of eight tree genera in an urban forest. To our knowledge, the potential of bi-temporal Pléiades imagery to discriminate urban tree species has never been assessed. Indeed, given the financial cost of this imagery, the additional contribution to classification performance of bi-temporal images needs to be tested. Pixel-based approaches were traditionally used to differentiate tree species, based on the difference in spectral values of individual pixels. However, when using VHR imagery, individual pixels may be classified differently from directly adjacent pixels (i.e., “salt-and-pepper effect”), resulting in high spectral variability within a class [18–20]. Object-based approaches use image objects rather than pixels as the smallest classification units and thus can overcome this issue. In addition, object-based methods offer the possibility to use features such as contrast, shape and correlation relationships, and improvement of classification accuracies compared to pixel-based approaches have been shown in many studies [21,22].

In this study, we aimed to (i) assess the potential of bi-temporal VHR Pléiades images for tree species classification in urban areas with an object-based method, and (ii) provide an exhaustive list of tree species used by the ring-necked parakeet to nest in the study area. As part of the case study, we

were also interested to compare the classification results of two machine-learning algorithms, Support Vector Machine (SVM) and Random Forest (RF) and to identify which Pléiades features contribute most to the classification accuracy.

2. Materials and Methods

2.1. Study Area

This study was carried out in the downtown and suburban part of Marseille, France. Located in the southeast of France, Marseille is the second most populous city in the country with an estimated human population of 855,000. The climate is Mediterranean, characterized by warm and dry summers, and rainy period in winter [23]. The city is surrounded by calcareous massifs at the north, east, and south. Despite a high density of built-up areas, the city displays a large amount of green spaces shaped by the history of the city [24] and a dense network of waterways. The study area corresponds to the spatial overlap of the Pléiades images used to perform the tree species classification with a total of 97 km² within the city of Marseille (Figure 1). Among the 62,799 individual trees of the public space inventoried by the city of Marseille in the study area, the species of 31,504 trees are unknown (i.e., more than 50%) and the other 31,295 belong to 112 different species.

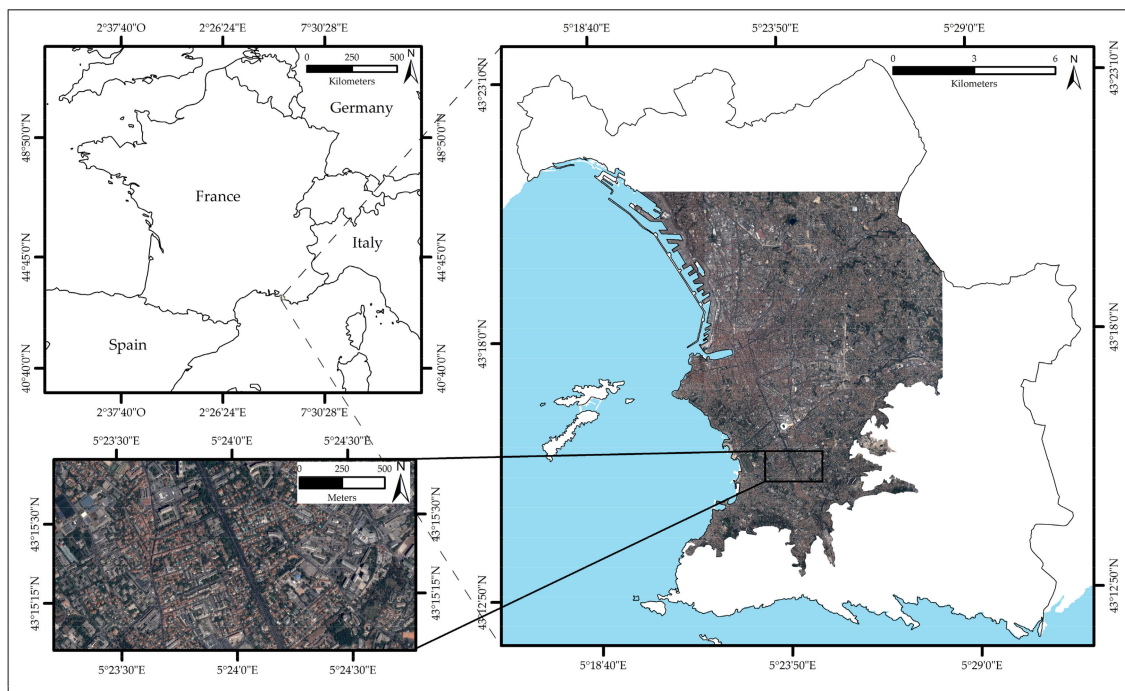


Figure 1. Location of the study area within the city of Marseille (right) in France (upper left) and zoom over the study area (lower left).

2.2. Datasets

2.2.1. Pléiades Images

The Pléiades constellation of two VHR satellites, Pléiades 1A and Pléiades 1B, was launched in 2011 under the supervision of the Centre National d'Etudes Spatiales (CNES) and Airbus Defence & Space. Cloud-free Pléiades images acquired on 28 July 2015 and 24 March 2016 were used in this study. The acquisition dates of images were selected based on both data availability and the vegetation phenology period in Mediterranean region. The Pléiades images have four multi-spectral bands with a spatial resolution of 2 m and one panchromatic band at 0.5 m (Table 1). Both Pléiades images were acquired pan-sharpened at 0.5 m spatial resolution. Atmospheric corrections were

applied using the Optical Calibration module implemented in the Orfeo ToolBox [25]. This step allows one to convert pixel values from digital numbers to physically interpretable and comparable spectral reflectance values, and requires one to set several parameters. The Optical Calibration module internally computes Top-of-Atmosphere reflectivity in the first step and Top-of-Canopy reflectance in the second step. The acquisition parameters, solar illumination and sensor gains, were obtained from Pléiades products metadata. After visual checking of the results of iterative tests, the continental aerosol model and the default parameter of the windows radius for adjacency effects correction were used. When using multi-temporal images, location displacement of trees may be caused by the differences in image acquisition time and the observation angle of the satellite. The early spring Pléiades image (from March) and the high summer Pléiades image (from July) were co-registered such that the co-registration error, i.e., Root Mean Square Error, was <0.5 pixel.

Table 1. Details of Pléiades imagery used for the urban tree species classification.

Title 1	Pléiades 1 28 July 2015	Pléiades 2 24 March 2016
PAN-MS resolution (m)	0.5–2	0.5–2
Panchromatic	470–830 nm	470–830 nm
Blue (B)	430–550 nm	430–550 nm
Green (G)	500–620 nm	500–620 nm
Red (R)	590–710 nm	590–710 nm
Near infra-red (NIR)	740–940 nm	740–940 nm
Solar azimuth	144	156
Solar elevation	62	46

2.2.2. Reference Data

Field surveys were conducted from June to August 2016 and June 2017 during the leaf-on period. The study area was divided into a regular grid of 1 km² square cells, then ten cells were randomly sampled. Within each of the ten cells, we registered broadleaf species composition by geo-referencing the localization and recording the species of individual trees. Coniferous trees were geo-referencing without details about the species of individuals. The four target tree species were chosen based on their dominance in the broadleaf vegetation community in the study area and their previously documented use by nesting ring-necked parakeets. Table 2 provides details on the final dataset.

Table 2. Reference samples from June to August 2016 and June 2017.

Classes	Number of Polygons	Number of Pixels
<i>Platanus</i> sp.	101	4520
<i>Tilia</i> sp.	644	3095
<i>Celtis</i> sp.	1032	5282
<i>Quercus</i> sp.	233	1544
Coniferous trees	479	7452
Other broadleaf species	281	9548

Figures 2 and 3 illustrate the spectral variability of the reflectance values for the six classes within the delineated reference polygons, respectively, of the spring and summer Pléiades images. The main difference between the coniferous and the broadleaf species are their reflectance in the near infrared band (NIR) of the summer image (Figure 3), the coniferous species having a lower reflectance value. Among the broadleaf trees group, some species significantly differ from the other. In the spring image (Figure 2), *Tilia* sp. consistently differs from the other broadleaf trees, with higher values in the four bands, whereas the separability of this species in the four bands of the summer image is less clear. Several species showed spectral overlaps, for example *Platanus* sp. and *Celtis* sp. in the red and green bands of the summer image.

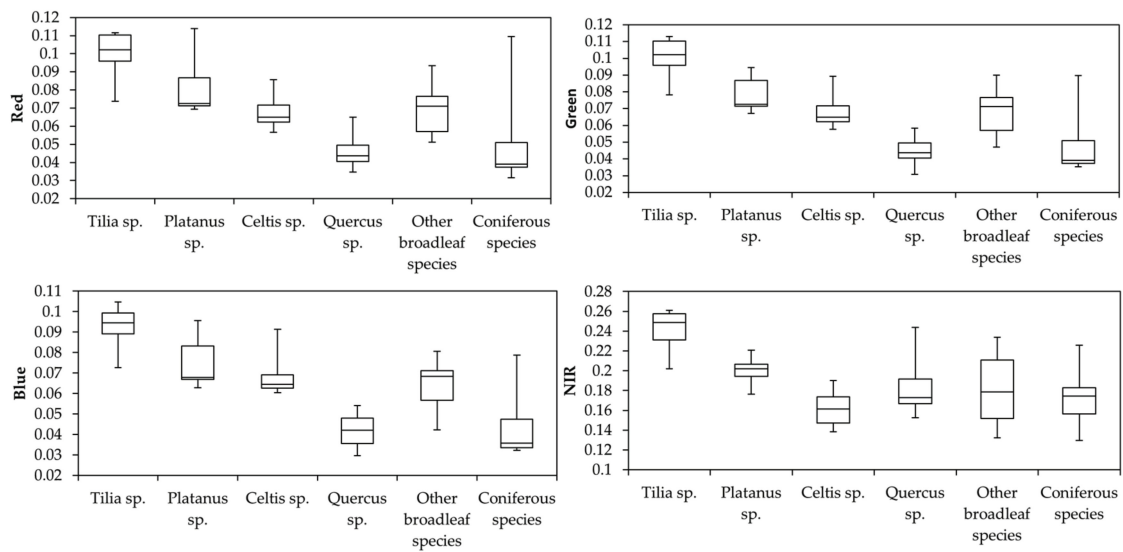


Figure 2. Mean spectral values within each of the spring Pléiades image spectral bands of the six classes over the study area.

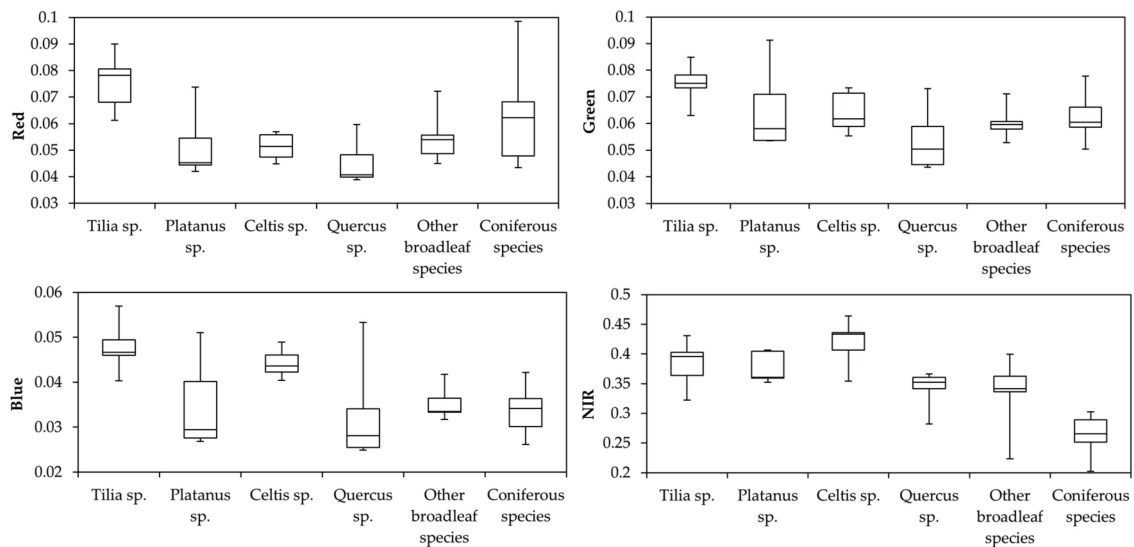


Figure 3. Mean spectral values within each of the summer Pléiades image spectral bands of the six classes over the study area.

2.3. Methodology

Figure 4 presents the flowchart of the classification procedure using an object-based method and two machine learning algorithms. The procedure consists of four steps: (1) data pre-processing (detailed in Section 2.2.1), (2) image segmentation, (3) feature extraction, and (4) object-based classification using SVM and RF. In this study, only nadir-visible trees were considered as the spectral information of trees obscured by shadows (i.e., from buildings) is difficult to obtain.

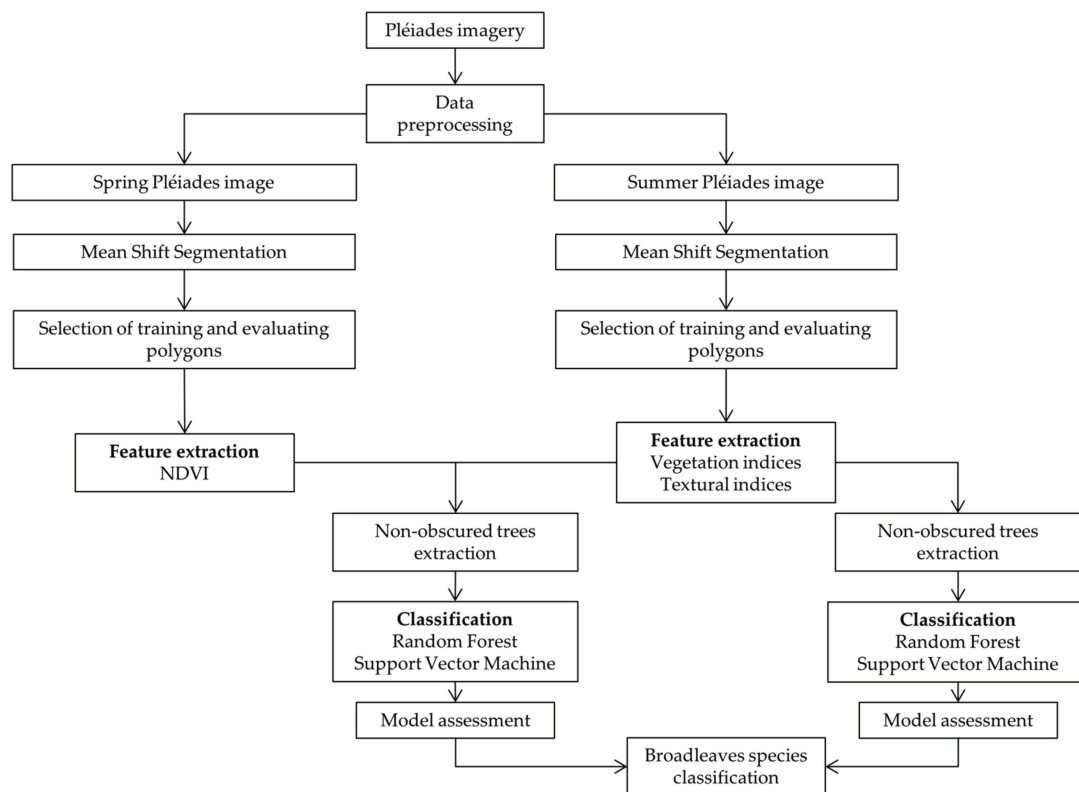


Figure 4. Workflow of the urban tree species classification procedure using the Pléiades imagery.

2.3.1. Segmentation

Segmentation is an important primary step in object-based classification which consists of dividing an image into homogeneous and non-intersecting regions. In this study, we used the mean shift algorithm, a non-parametric feature space analysis and clustering technique introduced by Fukunaga and Hostetler [26] and that has been widely applied for image segmentation [27,28]. We applied the Large Scale Mean Shift (LSMS) segmentation algorithm implemented in the open-source software Orfeo ToolBox and which requires assigning three parameters, the spatial radius of the neighborhood, the range radius, and the minimum region size. The optimum segmentation parameters depend on the scale and on the nature of the features to be detected. Segmentation performances were evaluated using Hoover metric (H) [29], which compares segmentation outcomes with ground truth regions based on an overlap matrix.

$$H = 1 - \frac{CD}{Ngt}, \quad (1)$$

where CD represents correct detections and N the total number of segments in the Ground Truth (gt).

A segment could be classified into five categories: correct detection, over-segmentation, under-segmentation, missed, and noise. Following Jiang et al. [30], we set the H threshold to 0.8 to define a segment correctly detected. For both Pléiades images, the final parameters were (1) spatial radius = 10, (2) range radius = 50, and (3) minimum region size = 10 (Figure 5).

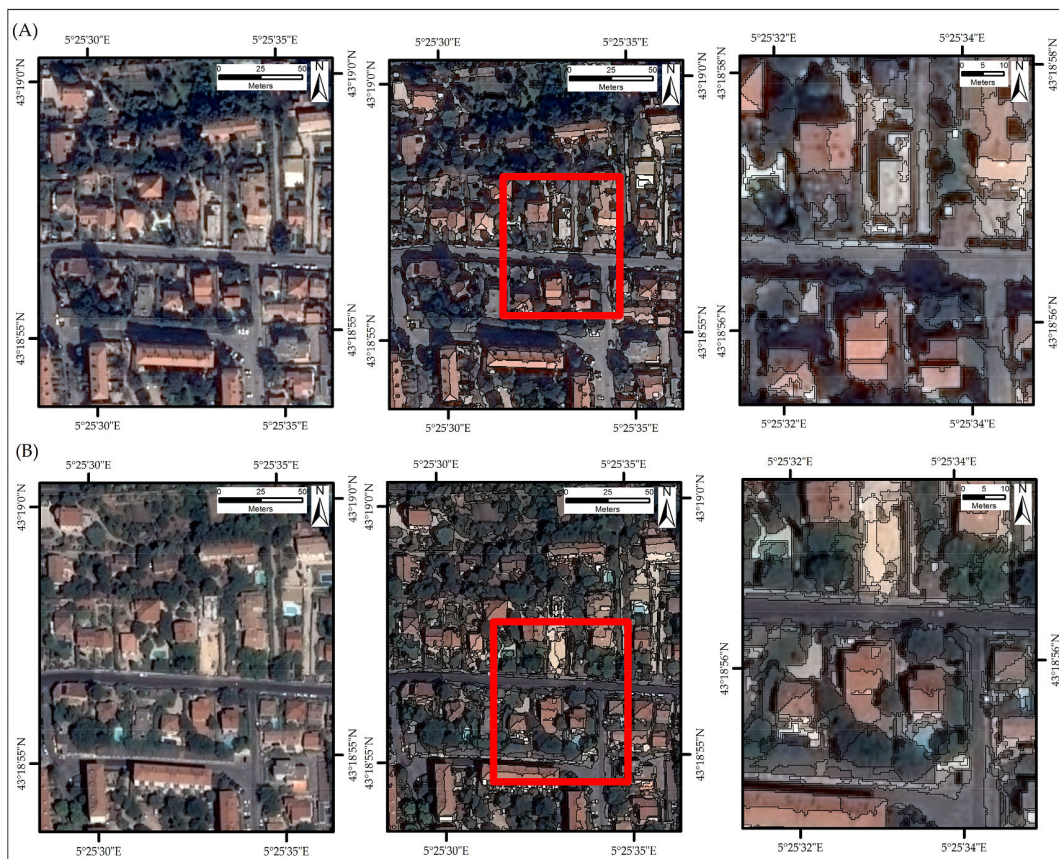


Figure 5. Segmentation results over (A) the spring Pléiades image and (B) the summer Pléiades image. Right images show a higher level of details for which the extent is displayed by the red squares.

2.3.2. Extraction of Spectral and Textural Features

Feature extraction may improve the classification results by expanding the image information. Combining multispectral and textural features may improve classification accuracy [31] and considering pixels about their immediate neighborhood rather than pixels in isolation should yield improved results, as demonstrated by Agüera et al. [32], Puissant et al. [33], and Chiu and Couloigner [34]. For both Pléiades images, a total of 91 features were extracted and computed at object level from the four spectral bands. Several studies have shown that Principal Component Analysis (PCA) may improve the classification results in urban areas [35]. PCA was performed using the four spectral bands and the first principal component of each image, which accounts for 63% of the variance in the summer Pléiades and 61% of the variance in the spring Pléiades image, was included. Spectral features consisted of means and variances of surface reflectance of each of the four spectral bands, Normalized Difference Vegetation Index (NDVI), and mean of the first principal component image. Textural features represent the measure of the regularity, the smoothness, and the coarseness of an image. Texture contained in VHR satellite imagery should contain useful information to extract regions of vegetation from an image as demonstrated by Tsai and Chou [36] who applied the Grey Level Co-Occurrence Matrix (GLCM) to Quickbird imagery to detect invasive plant species. We used the GLCM, one of the most widely used texture measures and first introduced by Haralick et al. [37]. The GLCM computes a matrix based on the difference between the grey levels of neighboring pixels within an image window of a given size, the size of which depending on the image resolution and the features being classified. Following the approach of Chen et al. [38], and Franklin et al. [39], both Pléiades was classified based on a range of GLCM window sizes. We used the Feature Extraction module implemented in Orfeo ToolBox. Feature measures fall into three categories: contrast based,

statistically based, and orderliness based. Given that textural features in the same category may be highly correlated [40], multicollinearity was evaluated using the Pearson Correlation Coefficient r , which ranges from +1 to -1. Values of r greater than +0.7 and lower than -0.7 indicate, respectively, strong positive and strong negative correlations between considered pairwise features and thus redundancy in information. Pairwise correlations with an r value greater than 0.7 were considered as correlated and one feature selected. Table 3 summarizes the 54 final spectral and textural features datasets. Appendix A, Table A1 summarizes the Pearson's values between features.

Table 3. Description of features extracted from spring and summer Pléiades images and used for the classification.

Feature Name	Description	Pléiades Image
Mean1-4	Mean of spectral bands 1-4	Spring and summer
Var1-4	Variance of spectral bands 1-4	Spring and summer
NDVI	Normalized Difference Vegetation Index NIR-R/NIR + R	Spring and summer
Entropy (entro1-4)	Measure of the randomness of the intensity distribution of spectral bands 1-4 $-\sum_{i,j}g(i,j)\log_2g(i,j)$, or 0 if $g(i,j) = 0$	Summer
Correlation (cor1-4)	Linear dependency of grey level values in the co-occurrence matrix of spectral bands 1-4 $\sum_{i,j}g(i,j)(i - \mu_x)(j - \mu_y)/\sigma_x\sigma_y$	Summer
Cluster Shade (clusha1-4)	Measure of the skewness of spectral bands 1-4 $\sum_{i,j}((i - \mu) + (j - \mu))^3g(i,j)$	Summer
Cluster Prominence (clupro1-4)	Measure of the asymmetry of spectral bands 1-4 $\sum_{i,j}((i - \mu) + (j - \mu))^4g(i,j)$	Summer
Haralick Correlation (harcor1-3)	Measure of correlation of spectral bands 1-3 $\sum_{i,j}(i,j)g(i,j) - \mu^2/\sigma^2$	Summer
Dissimilarity (dis1-4)	Spectral bands 1-4 $\sum_{i,j}(i - j)g(i,j)^2$	Summer
Information Measure of Correlation 1 (IC1-4)	Spectral bands 1-4 $H_{xy} - H_{xy1}/\max(H_x, H_y)$	Summer
Sum Variance (SVar1-4)	Spectral band 4 $\sum_{k=2}^{2N}(k - H_{x+y})g_{i+j}(k)$	Summer
PCA1	Mean of the first component from Principal Component Analysis	Spring and summer

With: $g(i,j)$ a normalized element of the GLCM matrix; μ_x ; μ_y and σ_x ; σ_y the means and standard deviations expressed as: $\mu_x = \sum_{i,j} ig(i,j)$, $\mu_y = \sum_{i,j} jg(i,j)$, $\sigma_x = \sqrt{\sum_{i,j} (i - \mu_x)^2 g(i,j)}$, $\sigma_y = \sqrt{\sum_{i,j} (i - \mu_y)^2 g(i,j)}$.

2.3.3. Classification and Tree Cover Mask

In the field of remote sensing, two major classifiers have been widely used due to their excellent classification results and the speed of processing: Random Forest (RF) and Support Vector Machine (SVM) [41,42]. The RF classifier yields reliable classifications using predictions derived from an ensemble of classification and regression trees (CARTs). The trees are created by drawing a subset of training samples through replacement which means that the same sample can be selected several times, while others may not be selected at all. RF produces an estimate of the generalization error using the Out-Of-Bag (OOB) samples. Relative feature importance is automatically calculated as Mean Decrease Accuracy (MDA) through random permutation. We used default parameters, which provide good classification results in tree species classification [43], and set the number of trees to be grown to 500 and the number of features used in each split was set equal to the square root of the total number of input features. The Support Vector Machine (SVM) classifier is a supervised non-parametric statistical learning method [44] which makes no assumption about the underlying data distribution (for a review, see Mountrakis et al. [41]). The SVM algorithm separates a given set of labeled training data with a hyperplane which finds the maximum distance. We used a Gaussian Radial Basis Function (RBF) kernel which has shown good performances in object-based image analysis [45,46]. Optimal cost and gamma values were determined by the grid search function in the R package e1071. We used the package randomForest [47] in the open-source software R 3.1.3 to perform RF models, and the SVM was implemented using the package e1071 [48]. A cross-validation technique was used to assess the

performances of models. The reference sample is randomly split into k subsets of equal size, $k-1$ subsets are then used as training data, and the remaining subset is used as validation data. Each k subset is used once as the validation data, and the k -fold cross-validation is repeated k times. This technique allows one to use the entire reference sample for both training and validating the models. We used the common 10-fold cross validation for both classifiers and for both single-date and bi-temporal classification [49]. Three accuracy measures, the overall accuracy (OA), kappa value (k), user's accuracy (UA), and producer's accuracy (PA), were used to assess the accuracy of models. PA corresponds to the error of omission (pixels that belong to a class but fail to be classified into this class), UA measures the error of commission (pixels that belong to a class but are labeled as belonging to another), and OA summarized the total classification accuracy. A model's accuracy is considered as poor for a Kappa coefficient value below 0.20, moderate between 0.40 and 0.60, and beyond 0.80 means almost perfect [50]. McNemar's test was used to evaluate the statistical significance of the observed differences in the overall and class-specific accuracies of single-date and bi-temporal classifications using the same reference sample [51]. This non-parametric test evaluates the differences between paired proportions and the difference between the two classifications is significant when the p -value is less than 0.05.

Extraction of tree- and non-tree objects was made using a two-step process. In the first step, we mask buildings and water objects using the thematic layers of BDTopo[®], acquired in December 2014 and provided by the National Institute of Geographic and Forestry Information (IGN), and agricultural and herbaceous areas using thematic layers acquired in June 2015 and provided by the intercommunal structure Aix-Marseille-Provence Metropolis. This step allows one to avoid potential spectral overlap between vegetation and, for example, green roofs. In the second step, we used an NDVI threshold to extract tree objects. Histogram analysis of the NDVI band from the summer image was used to estimate NDVI threshold as 0.6. All the objects with mean NDVI values lower than this threshold are thus removed. It should be noted that the purpose of using an NDVI threshold in this study was only to differentiate trees and background, and not to determine the phenology of species.

2.3.4. Ring-Necked Parakeet Breeding Occurrences

Breeding site locations of ring-necked parakeets in the study area were compiled from the database of the regional antenna of the French Bird Protection League, a national network which compiles observations made by volunteers (Collectif, in <http://www.faune-paca.org>, subject to a convention and extracted on December 2016). The dataset was composed by 1830 parakeet breeding occurrences for the period 2009–2016.

3. Results

3.1. Classification Results

Table 4 lists the accuracy measures including the average overall accuracy (OA) and kappa values from single-date and bi-temporal images at the study area. The OA ranges from 64.1% to 79.2% and Kappa values from 0.53 to 0.72. Using either the SVM or RF algorithm, tree species classification based on bi-temporal Pléiades images produces higher accuracies than those based on the single-date image. When using bi-temporal images, the OA and the kappa values are respectively 11.5–13.9% and 0.12–0.17 higher compared to classification using single-date image.

Table 4. Accuracy measures for the urban tree species classification using SVM and RF with single-date and bi-temporal Pléiades images. SVM: Support Vector Machine; RF: Random Forest; OA: Overall Accuracy.

	SVM		RF	
	OA (%)	Kappa	OA (%)	Kappa
Single-date (using Spring Pléiades image)	64.1	0.53	65.3	0.55
Bi-temporal Pléiades images	75.6	0.65	79.2	0.72

3.2. Relative Importance of Features

The MDA (Table 5) and the F-score (Table 6) highlight the feature importance in the single-date and the bi-temporal classification, respectively, in the RF and the SVM models. Textural measure of correlation in the blue band (Summer_IC3, Table 5) and in the green band (Summer_Cor2, Table 6) were the most important features in the single-date classification, followed by spectral features in the blue and the NIR bands (Summer_Mean3 and Summer_Mean4, Table 5) for the RF model and only in the blue band (Summer_Mean3, Table 6) for the SVM model. When using bi-temporal images, the textural measure of correlation in the summer image red band (Summer_IC1, Table 5) followed by spectral information in the spring image NIR band (Spring_Mean4) were the most important features in the RF model. In the SVM model, measures of entropy in the summer green band (Summer_Entro2, Table 6) and correlation in the summer red band (Summer_Cor1) were the two most important features.

Table 5. Mean Decrease Accuracy values of the ten most important features in the single-date classification and the bi-temporal classification using RF algorithm.

Mean Decrease Accuracy			
Features	Single-Date	Features	Bi-Temporal
Summer_IC3	25.1	Summer_IC1	24.9
Summer_Mean3	24.3	Spring_Mean4	22.8
Summer_Mean4	23.4	Summer_IC3	18.9
Summer_IC1	21.9	Spring_Mean3	18.5
Summer_Cor4	20.4	Summer_IC2	18.4
Summer_Cor1	19.8	Summer_Cor4	18.1
Summer_Entro2	19.7	Summer_Cor1	17.9
Summer_Dis4	18.7	Summer_PCA1	17.8
Summer_SVar4	18.6	Spring_Var4	17.8
Summer_Clupro4	18.4	Spring_SVar4	17.5

Table 6. F-score values of the ten most important features in the single-date classification and the bi-temporal classification using SVM algorithm.

F-Score (%)			
Features	Single-Date	Features	Bi-Temporal
Summer_Cor2	79.1	Summer_Entro2	77.9
Summer_Mean3	53.4	Summer_Cor1	50.4
Summer_Entro2	48.5	Summer_Dis3	42.9
Summer_IC3	42.4	Summer_IC4	39.4
Summer_Cor3	42.3	Summer_Dis2	38.9
Summer_Cor1	37.4	Summer_IC3	35.7
Summer_Dis2	36.1	Summer_Cor2	35.4
Summer_Mean1	32.4	Summer_Entro4	34.8
Summer_NDVI	32.1	Spring_Var4	31.4
Summer_Var4	28.9	Spring_Mean3	31.2

3.3. Tree Species Classification

The confusion matrices in Table 7 summarize the results for the tree species classification based on 10-fold cross-validation using RF in single-date and bi-temporal classifications. The producer's accuracies ranged from 27.9% (*Quercus* sp.) to 87.1% (*Tilia* sp.) in the single-date classification and ranged from 33.4% (*Quercus* sp.) to 100% (coniferous species) in the bi-temporal classification. The user's accuracies ranged from 44.6% (other broadleaf species) to 100% (coniferous species and *Quercus* sp.) in the single-date classification and ranged from 54.9% (*Platanus* sp.) to 100% (coniferous species and *Quercus* sp.) in the bi-temporal classification. With the exception of *Quercus* sp., bi-temporal images significantly improved ($p < 0.05$) the discrimination between the different species of broadleaf

trees with increases of the producer's accuracies of all species. The most problematic class was *Quercus* sp., achieving only PA around 28% in the single-date classification and 33% in the bi-temporal classification with no significant difference found according to the McNemar test. When using bi-temporal Pléiades images, the coniferous and broadleaf tree species were perfectly separated (100% coniferous trees correctly classified). The preeminence of bi-temporal classification is supported by the result of McNemar's test with significant difference found when using RF algorithm ($p < 0.05$).

Table 7. Confusion matrices and statistical measures for the tree species classification with single-date and bi-temporal Pléiades images using Random Forest algorithm. UA: User's accuracy, PA: Producer's accuracy.

Single-Date Classification								
Reference Data								
Classified as	<i>Platanus</i> sp.	<i>Tilia</i> sp.	<i>Celtis</i> sp.	<i>Quercus</i> sp.	Coniferous Species	Other Broadleaf Species	Σ	UA (%)
<i>Platanus</i> sp.	82	21	5	0	0	37	145	56.5
<i>Tilia</i> sp.	15	561	404	127	0	132	1239	45.3
<i>Celtis</i> sp.	4	38	598	40	0	4	684	87.4
<i>Quercus</i> sp.	0	0	0	65	0	0	65	100
Coniferous species	0	0	0	0	395	0	395	100
Other broadleaf species	0	24	25	1	84	108	242	44.6
Σ	101	644	1032	233	479	281	2770	
PA(%)	81.2	87.1	57.9	27.9	82.5	38.4		65.3
Kappa								0.55
Bi-Temporal Classification								
Reference Data								
Classified as	<i>Platanus</i> sp.	<i>Tilia</i> sp.	<i>Celtis</i> sp.	<i>Quercus</i> sp.	Coniferous Species	Other Broadleaf Species	Σ	UA (%)
<i>Platanus</i> sp.	83	7	35	0	0	26	151	54.9
<i>Tilia</i> sp.	18	606	164	120	0	125	1033	58.7
<i>Celtis</i> sp.	0	15	819	32	0	0	866	94.6
<i>Quercus</i> sp.	0	0	0	78	0	0	78	100
Coniferous species	0	0	0	0	479	0	479	100
Other broadleaf species	0	16	14	3	0	130	163	79.7
Σ	101	644	1032	233	479	281	2770	
PA (%)	82.2	94.1	79.4	33.5	100	46.3		79.2
Kappa								0.72
McNemar's test significance	NS	***	***	NS	***	**		***

NS: $p > 0.05$. * $p < 0.05$. ** $p < 0.01$. *** $p < 0.001$.

We classified the study area with the object-based RF models using single-date Pléiades image and bi-temporal Pléiades images. Figure 6 displays two levels of detail for both the single-date (Figure 6A) and the bi-temporal classification (Figure 6B). The classification of *Celtis* sp. using bi-temporal images corresponded well to the field survey observations, with a large dominance of this species in the road-street alignments. The improvement of differentiation between *Tilia* sp. and *Celtis* sp. is showed in higher detail between the single-date classification (upper right) and the bi-temporal classification (lower right).

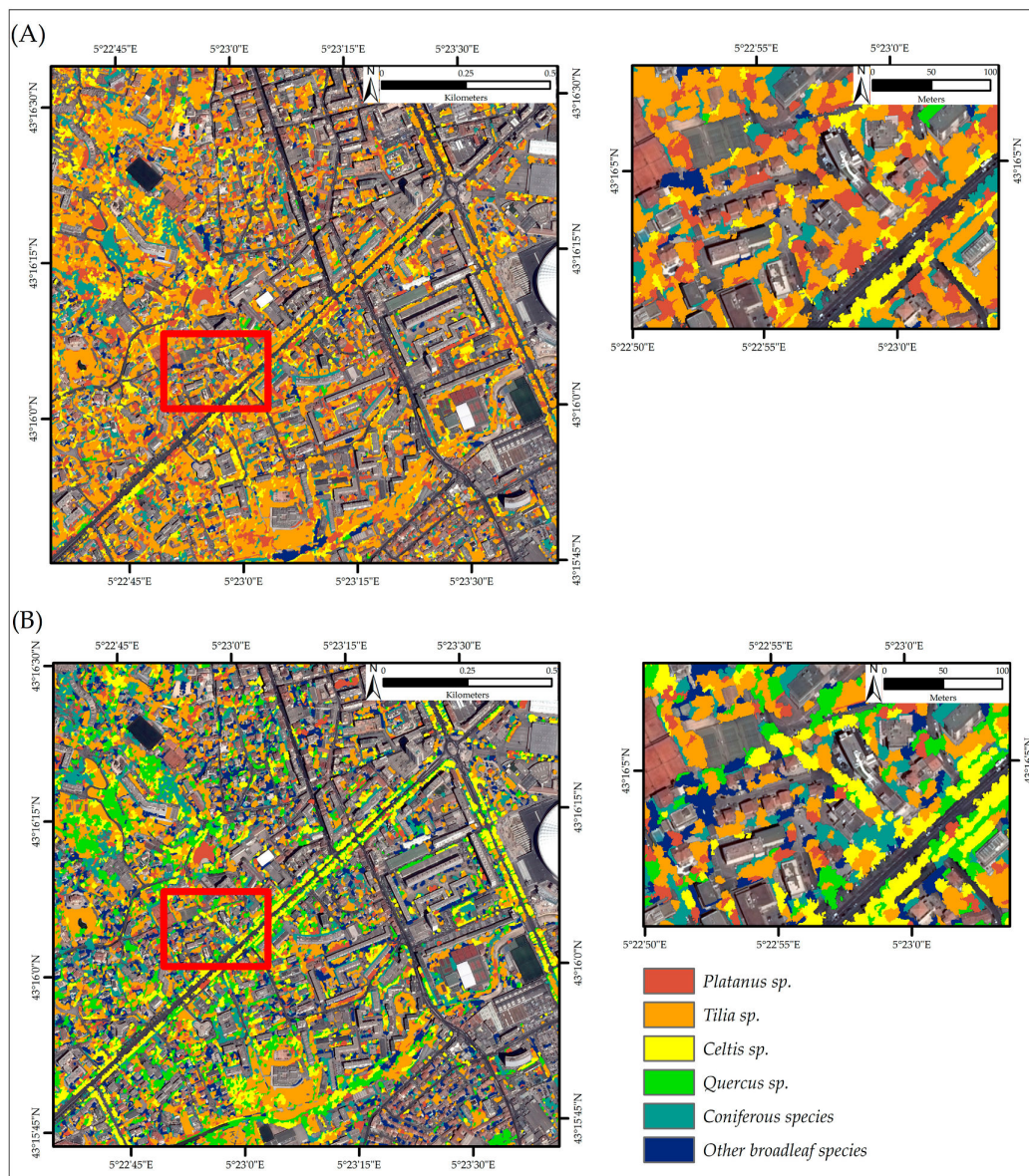


Figure 6. Classification maps based on object-based RF model using (A) single-date Pléiades image and (B) bi-temporal Pléiades images.

3.4. Relative Use of Tree Species by Nesting Ring-Necked Parakeets

Table 6 summarized the tree species classified using RF in bi-temporal Pléiades images and used as nest sites by the ring-necked parakeet in the study area in Marseille, France. RF classification allows one to identify 98.5% of the tree species used by the ring-necked parakeet for nesting. The most used tree species is *Platanus* sp. in which 95% of the parakeets' nests are found. A very low proportion of parakeet nests is also found in *Quercus* sp. and *Tilia* sp.

4. Discussion

4.1. Contribution of Bi-Temporal Pléiades Images on Urban Tree Species Classification

In this study, we evaluated the potential of bi-temporal Pléiades images for tree species classification in a Mediterranean city of France, Marseille. To our knowledge, this is the first time that a study has assessed the additional contribution of using more than one Pléiades image in tree species

classification. We applied an object-based approach with two machine learning algorithms, SVM and RF, using either solely summer Pléiades image or using both spring and summer Pléiades images. Bi-temporal classification achieved overall accuracies 11.5–13.9% higher compared to single-date image classification with significant differences in overall and class-specific accuracies found when using RF algorithm. Producer's and User's accuracy were also more balanced. In comparison with previous studies, we only used images representing two seasons, spring and summer. Tigges et al. [17] recommend the use of three seasons, spring, summer, and autumn, to discriminate tree species with the highest accuracy in urban areas. Li et al. [16] combined two WorldView images, acquired in late summer and high autumn, for identifying tree species in Beijing, China. They achieved good classification results with an overall accuracy of 92.4% using bi-temporal images. Our results confirm these findings by combining images acquired in early spring and high summer and highlight the additional contribution of Pléiades bi-temporal images in the discrimination between coniferous and broadleaf species, and between the different species of broadleaf trees. The higher accuracy of the bi-temporal models may be attributed to the use of the spring image during the process, representing the differences in the phenological patterns among tree species and thus helped to improve their separability. Indeed, the development of leaves from early spring to summer leads to an increase of the content of chlorophyll in the leaves' cells. As shown by the difference between spectral reflectance values in Figures 2 and 3, this phenological process results in a decrease of reflectance in the blue and red bands and an increase in the NIR band. In our study, a clear distinction between coniferous and broadleaf species was made using bi-temporal images. As shown in Figure 3, coniferous species traditionally exhibit lower reflectance values in the NIR spectrum in comparison with broadleaf species, due to their particular structure of leaves with less chlorophyll contained in their cells [52]. The feature importance analysis (Tables 5 and 6) confirms the high contribution of the spring NIR band in the bi-temporal models. Using both spring and summer images particularly improves the separability between *Tilia* sp. and *Celtis* sp. As shown in Figure 2A, *Tilia* sp. displays significant differences of the reflectance values in the four spectral bands of the spring images in comparison with the other broadleaf trees. This may be due to its specific phenological pattern, especially in the Mediterranean region, with the presence of early leaves on *Tilia* sp. at the beginning of the spring season, while leaves are not yet developed on the other broadleaf species. The most problematic class was *Quercus* sp., with producer's accuracies only equal to 27.9% in the single-date classification and 33.5% in the bi-temporal classification. This may be explained by the low number of reference polygons for this class, the lowest among all classes, and thus the difficulty in characterizing the spectral variability of individuals trees according to their different phenological stages or ages along the urban gradient. Regarding the relative contribution of features extracted from both Pléiades images, textural and spectral information contributed differently according to the classification scheme. When using the single-date image, textural features in the green and the blue bands and spectral information in the blue and the NIR bands were the most important features. When using bi-temporal images, textural features in the four bands of the summer image and spectral information in the NIR and blue bands of the spring image were among the most important features. The importance of the blue band has previously been highlighted by several studies using Pléiades imagery [53] and its importance in classifying coniferous species due to their low photosynthetic activity in the blue light [54]. Unexpectedly, the NDVI band of the spring image was not among the most important features, regardless of the classifiers used. As pointed out by Sheeren et al. [55], who found similar results in temperate forests in southwest France, NDVI is, by definition, correlated to the red and NIR bands and that more information is found in these bands. Achieving an overall accuracy of 79.2%, our bi-temporal RF model supports that the combination of textural and spectral features lead to satisfactory results as shown by previous studies [39,56]. In this study, we only used textural features extracted from the summer image. As computing power can be a major limitation in the classification of tree species in large areas such as a city, the good accuracy of our model suggests that these features may be sufficient. However, further comparative research

should investigate the additional contribution of textural information extracted from other seasons with different ages of leaves.

4.2. Random Forest and Support Vector Machine Algorithms

We tested two classification algorithms for classifying the image objects, Random Forest and Support Vector Machine, to ensure that the improvement of bi-seasonal images in urban tree species classification is independent of the classification approaches used. Most studies that used these classifiers in tree species classification found that they achieve good performances with high accuracies [16]. Studies that have compared SVM and RF in various classification applications found very different results. For example, Pal [57] found that these two algorithms perform equally well for land cover classification using Landsat data while Li et al. [16] compared SVM and RF for tree species classification and found that SVM systematically outperforms RF. In this study, we found that RF slightly outperforms SVM regardless of the classification scheme, and we used RF results to identify tree species used by the ring-necked parakeet.

4.3. Spatial Distribution of Tree Species and Breeding Ring-Necked Parakeets across the City of Marseille

Figure 6 shows the spatial distribution of the different tree species mapped in this study. Scattered distribution of tree species may increase the potential of misclassification given that tree crowns may overlap between adjacent species. In our study, the most well-classified tree species was *Celtis* sp., which is increasingly used in Marseille as road street trees. Its uniform distribution thus reduces the effect of different species crown overlap. The ring-necked parakeet is a cavity-nesting bird widely introduced in European cities. In its introduced range, this parakeet already showed its preference for the genus *Platanus* in many cities. *Platanus* sp. trees host more than the half of the broods in the Upper Rhine Valley [58] and 66% in Heidelberg city, Germany [59], 78% in the Ile-de-France region, France [60], and 62% in Sevilla, Spain [61]. Tree species classification performed in this study allowed identification of 98.5% of all tree species used by nesting ring-necked parakeets (Table 8). To our knowledge, this is the first time that remote sensing has been used to study potential nesting preferences of bird species. The tree species used as nesting sites by ring-necked parakeets in Marseille matches the literature, our results showed that the majority of the nests are found in *Platanus* sp. trees. The extensive use of *Platanus* tree cavities by the ring-necked parakeet has mainly been attributed to the highest number of cavities found in this tree species and to the dominance of *Platanus* sp. trees in urban tree communities. Our methodology does not allow us to assess the proportion of individual *Platanus* sp. trees in the study area, even if we found that it is not the most abundant species in terms of coverage. In the city of Marseille, *Platanus* sp. trees have been extensively planted as road/street trees and for ornamental aims. However, it is affected by a fungus, *Ceratocystis platani*, responsible for the lethal canker stain disease which will require urban planners to cut the dying individuals and replace them with others such as *Celtis australis*. This species turn-over may have a high impact on biodiversity because of the progressive decrease of cavity availability due to the newly-planted young trees. Cavity availability is a major element of competition and shapes the species composition within the cavity-nesters community inside cities. The presence of old and large trees is critical for the subsistence of animal species such as owls, bats, and other cavity-nesters. Databases of areas with suitable trees are thus crucially needed to study their spatial distribution and may be a useful tool to biodiversity-friendly urban planning. A supplementary step after the classification of tree species may allow one to obtain information on the age of individual trees and used as a proxy for cavity availability. Methods using textural features, as proposed by Franklin et al. [62], represents a promising area to achieve this task.

Table 8. Tree species used as nest sites by ring-necked parakeets *Psittacula krameri* in Marseille, France.

	Number of Ring-Necked Parakeets Nests	Proportion (%)
<i>Platanus</i> sp.	1738	95
<i>Tilia</i> sp.	27	1.5
<i>Celtis</i> sp.	0	0
<i>Quercus</i> sp.	37	2
Coniferous trees	0	0
Other broadleaf trees	18	1
Other	10	0.50
Total	1830	100

5. Conclusions

In this study, our aim was to map the different tree species in a Mediterranean city of France to identify the tree species used by an introduced bird species, the ring-necked parakeet, as nest sites. Pléiades images were used and object-based classifications were performed using either a single-date image (acquired in summer) or bi-temporal images (acquired in spring and summer) with two classifiers, Random Forest and Support Vector Machine. The main conclusions derived from our study were:

- (1) Our results showed for the first time that bi-temporal Pléiades images improve the discrimination between coniferous and broadleaf tree species, and the discrimination between the different broadleaf tree species.
- (2) Our findings also suggest that the combination of textural and spectral information is important for discriminating tree species, and that textural features extracted during in-leaf seasons may be sufficient to achieve good classification accuracy.
- (3) Object-based classification represents a powerful tool to study the ecological requirements of fauna, especially in urban areas. Remote sensing techniques using open-source software such as Orfeo ToolBox may be particularly useful for invasive species management but also for the conservation of native fauna by highlighting ecological preferences regarding their breeding and feeding areas.

The *Platanus* sp. distribution map generated in this study will be used as an environmental predictor for the study of ring-necked parakeet population dynamics through Species Distribution Models (SDMs). One of the major issues of SDMs is to obtain environmental layers which are temporally coherent with the occurrence data of the target species. In our opinion, remote sensing is one of the most powerful and time/cost-friendly techniques which will enable the generation of spatio-temporally consistent species distribution models (SDMs) called by He et al. [63] the next-generation of SDM (NG-SDMs). In our opinion, researchers in the field of ecology and geography may gain great advantages by combining their knowledge and expertise to produce interdisciplinary research.

Acknowledgments: The authors would like to thank the anonymous reviewers who helped us improve this paper.

Author Contributions: M.L.L. and E.B. conceived and designed the experiments; M.L.L. performed the experiments; M.L.L. analyzed the data; and M.L.L., P.C. and M.D.C wrote the paper.

Conflicts of Interest: The authors declare no conflict of interest.

Appendix A

Table A1. Pearson’s correlation matrices for the features extracted from summer Pléiades image.

Summer Pléiades Image								
Band 1								
	Energy	Entropy	Correlation	Inverse Difference Moment	Inertia	Cluster Shade	Cluster Prominence	Haralick Correlation
Energy	1.00	−0.96	0.12	0.88	−0.57	−0.04	−0.38	−0.51
Entropy		1.00	0.22	−0.95	0.72	0.06	0.52	0.68
Correlation			1.00	0.40	−0.41	0.05	−0.12	−0.04
Inverse Difference Moment				1.00	−0.83	0.00	−0.53	−0.67
Inertia					1.00	−0.05	0.71	0.66
Cluster Shade						1.00	−0.07	−0.30
Cluster Prominence							1.00	0.55
Haralick Correlation								1.00
Band 2								
	Energy	Entropy	Correlation	Inverse Difference Moment	Inertia	Cluster Shade	Cluster Prominence	Haralick Correlation
Energy	1.00	−0.96	0.12	0.88	−0.57	−0.04	−0.38	−0.51
Entropy		1.00	−0.23	−0.95	0.72	0.02	0.51	0.66
Correlation			1.00	0.40	−0.41	0.04	−0.28	−0.28
Inverse Difference Moment				1.00	−0.83	0.00	−0.53	−0.67
Inertia					1.00	−0.05	0.71	0.66
Cluster Shade						1.00	−0.08	−0.31
Cluster Prominence							1.00	0.59
Band 3								
	Energy	Entropy	Correlation	Inverse Difference Moment	Inertia	Cluster Shade	Cluster Prominence	Haralick Correlation
Energy	1.00	−0.97	−0.07	0.89	−0.61	−0.07	−0.40	−0.53
Entropy		1.00	−0.04	−0.96	0.73	0.05	0.52	0.66
Correlation			1.00	0.22	−0.30	0.04	−0.20	−0.17
Inverse Difference Moment				1.00	−0.84	−0.04	−0.55	−0.67
Inertia					1.00	−0.04	0.71	0.67
Cluster Shade						1.00	−0.09	−0.30
Cluster Prominence							1.00	0.58
Band 4								
	Energy	Entropy	Correlation	Inverse Difference Moment	Inertia	Cluster Shade	Cluster Prominence	Haralick Correlation
Energy	1.00	−0.99	−0.46	0.96	−0.77	0.05	−0.57	−0.78
Entropy		1.00	0.41	−0.98	0.82	−0.05	0.62	0.80
Correlation			1.00	−0.30	0.13	−0.02	0.14	0.29
Inverse Difference Moment				1.00	−0.90	0.05	−0.64	−0.80
Inertia					1.00	−0.09	0.73	0.68
Cluster Shade						1.00	−0.09	−0.27
Cluster Prominence							1.00	0.55

References

1. Wilcove, D.S.; Rothstein, D.; Dubow, J.; Phillips, A.; Losos, E. Quantifying Threats to Imperiled Species in the United States: Assessing the relative importance of habitat destruction, alien species, pollution, overexploitation, and disease. *BioScience* **1998**, *48*, 607–615. [[CrossRef](#)]
2. Gurevitch, J.; Padilla, D.K. Are invasive species a major cause of extinctions? *Trends Ecol. Evol.* **2004**, *19*, 470–474. [[CrossRef](#)] [[PubMed](#)]
3. Blackburn, T.M.; Pyšek, P.; Bacher, S.; Carlton, J.T.; Duncan, R.P.; Jarošík, V.; Wilson, J.R.U.; Richardson, D.M. A proposed unified framework for biological invasions. *Trends Ecol. Evol.* **2011**, *26*, 333–339. [[CrossRef](#)] [[PubMed](#)]
4. Lockwood, J.L.; Cassey, P.; Blackburn, T. The role of propagule pressure in explaining species invasions. *Trends Ecol. Evol.* **2005**, *20*, 223–228. [[CrossRef](#)] [[PubMed](#)]
5. Forshaw, J.M. *Parrots of the World*; Princeton University Press: Princeton, NJ, USA, 2010.
6. Pârâu, L.G.; Strubbe, D.; Mori, E.; Menchetti, M.; Ancillotto, L.; van Kleunen, A.; White, R.L.; Luna, Á.; Hernández-Brito, D.; Le Louarn, M.; et al. Rose-ringed Parakeet Populations and Numbers in Europe: A Complete Overview. *Open Ornithol. J.* **2016**, *9*, 1–13. [[CrossRef](#)]
7. Peck, H.L.; Pringle, H.E.; Marshall, H.H.; Owens, I.P.F.; Lord, A.M. Experimental evidence of impacts of an invasive parakeet on foraging behavior of native birds. *Behav. Ecol.* **2014**, *25*, 582–590. [[CrossRef](#)] [[PubMed](#)]
8. Le Louarn, M.; Couillens, B.; Deschamps-Cottin, M.; Clergeau, P. Interference competition between an invasive parakeet and native bird species at feeding sites. *J. Ethol.* **2016**, *34*, 291–298. [[CrossRef](#)] [[PubMed](#)]
9. Clergeau, P.; Vergnes, A. Bird feeders may sustain feral Rose-ringed parakeets *Psittacula krameri* in temperate Europe. *Wildl. Biol.* **2011**, *17*, 248–252. [[CrossRef](#)]
10. Strubbe, D.; Matthysen, E.; Graham, C.H. Assessing the potential impact of invasive ring-necked parakeets *Psittacula krameri* on native nuthatches *Sitta europaea* in Belgium. *J. Appl. Ecol.* **2010**, *47*, 549–557. [[CrossRef](#)]
11. Newton, I. Experiments on the limitation of bird breeding densities: A review. *Ibis* **1994**, *136*, 397–411. [[CrossRef](#)]
12. Menchetti, M.; Mori, E.; Angelici, F.M. Effects of the Recent World Invasion by Ring-Necked Parakeets *Psittacula krameri*. In *Problematic Wildlife*; Angelici, F.M., Ed.; Springer International Publishing: Cham, Switzerland, 2016; pp. 253–266.
13. Robertson, M.P.; Cumming, G.S.; Erasmus, B.F.N. Getting the most out of atlas data. *Divers. Distrib.* **2010**, *16*, 363–375. [[CrossRef](#)]
14. Li, D.; Ke, Y.; Gong, H.; Chen, B.; Zhu, L. Tree species classification based on WorldView-2 imagery in complex urban environment. In Proceedings of the 2014 Third International Workshop on Earth Observation and Remote Sensing Applications (EORSA), Changsha, China, 11–14 June 2014; pp. 326–330.
15. Zipper, S.C.; Schatz, J.; Singh, A.; Kucharik, C.J.; Townsend, P.A.; Loheide, S.P., II. Urban heat island impacts on plant phenology: Intra-urban variability and response to land cover. *Environ. Res. Lett.* **2016**, *11*, 054023. [[CrossRef](#)]
16. Li, D.; Ke, Y.; Gong, H.; Li, X. Object-Based Urban Tree Species Classification Using Bi-Temporal WorldView-2 and WorldView-3 Images. *Remote Sens.* **2015**, *7*, 16917–16937. [[CrossRef](#)]
17. Tigges, J.; Lakes, T.; Hostert, P. Urban vegetation classification: Benefits of multitemporal RapidEye satellite data. *Remote Sens. Environ.* **2013**, *136*, 66–75. [[CrossRef](#)]
18. Dalponte, M.; Ørka, H.O.; Ene, L.T.; Gobakken, T.; Næsset, E. Tree crown delineation and tree species classification in boreal forests using hyperspectral and ALS data. *Remote Sens. Environ.* **2014**, *140*, 306–317. [[CrossRef](#)]
19. MacLean, M.G.; Congalton, R.G. Map accuracy assessment issues when using an object-oriented approach. In Proceedings of the American Society for Photogrammetry and Remote Sensing 2012 Annual Conference, Sacramento, CA, USA, 19–23 March 2012; pp. 1–5.
20. Blaschke, T.; Strobl, J. What's wrong with pixels? Some recent developments interfacing remote sensing and GIS. *Geo-Inf. Syst.* **2002**, *14*, 12–17.
21. Van Aardt, J.A.N.; Wynne, R.H. Examining pine spectral separability using hyperspectral data from an airborne sensor: An extension of field-based results. *Int. J. Remote Sens.* **2007**, *28*, 431–436. [[CrossRef](#)]
22. Voss, M.; Sugumaran, R. Seasonal Effect on Tree Species Classification in an Urban Environment Using Hyperspectral Data, LiDAR, and an Object-Oriented Approach. *Sensors* **2008**, *8*, 3020–3036. [[CrossRef](#)] [[PubMed](#)]

23. Aschmann, H. Distribution and Peculiarity of Mediterranean Ecosystems. In *Mediterranean Type Ecosystems*; di Castri, F., Mooney, H.A., Eds.; Springer: Berlin/Heidelberg, Germany, 1973; pp. 11–19.
24. Roncayolo, W. Les grammaires d'une ville. Essai sur la genèse des structures urbaines à Marseille. *Ann. Hist. Sci. Soc.* **1997**, *52*, 1195–1198.
25. Christophe, E.; Inglada, J.; Giros, A. Orfeo toolbox: A complete solution for mapping from high resolution satellite images. *Int. Arch. Photogramm. Remote Sens. Spat. Inf. Sci.* **2008**, *37*, 1263–1268.
26. Fukunaga, K.; Hostetler, L. The estimation of the gradient of a density function, with applications in pattern recognition. *IEEE Trans. Inf. Theory* **1975**, *21*, 32–40. [[CrossRef](#)]
27. Comaniciu, D.; Meer, P. Mean Shift: A Robust Approach toward Feature Space Analysis. *IEEE Trans. Pattern Anal. Mach. Intell.* **2002**, *24*, 603–619. [[CrossRef](#)]
28. Michel, J.; Youssefi, D.; Grizonnet, M. Stable Mean-Shift Algorithm and Its Application to the Segmentation of Arbitrarily Large Remote Sensing Images. *IEEE Trans. Geosci. Remote Sens.* **2015**, *53*, 952–964. [[CrossRef](#)]
29. Hoover, A.; Jean-Baptiste, G.; Jiang, X.; Flynn, P.J.; Bunke, H.; Goldgof, D.B.; Bowyer, K.; Eggert, D.W.; Fitzgibbon, A.; Fisher, R.B. An Experimental Comparison of Range Image Segmentation Algorithms. *IEEE Trans. Pattern Anal. Mach. Intell.* **1996**, *18*, 673–689. [[CrossRef](#)]
30. Jiang, X.; Marti, C.; Irniger, C.; Bunke, H. Distance Measures for Image Segmentation Evaluation. *EURASIP J. Appl. Signal Process.* **2006**, 209. [[CrossRef](#)]
31. Ruiz, L.A.; Fdez-sarria, A.; Recio, J.A. Texture feature extraction for classification of remote sensing data using wavelet decomposition: A comparative study. *Int. Arch. Photogramm. Remote Sens.* **2004**, *XXXV*, 1682–1750.
32. Agüera, F.; Aguilar, F.J.; Aguilar, M.A. Using texture analysis to improve per-pixel classification of very high resolution images for mapping plastic greenhouses. *ISPRS J. Photogramm. Remote Sens.* **2008**, *63*, 635–646. [[CrossRef](#)]
33. Puissant, A.; Hirsch, J.; Weber, C. The utility of texture analysis to improve per-pixel classification for high to very high spatial resolution imagery. *Int. J. Remote Sens.* **2005**, *26*, 733–745. [[CrossRef](#)]
34. Chiu, W.Y.; Couloigner, I. Evaluation of incorporating texture into wetland mapping from multispectral images. *EARSeL EProc.* **2004**, *3*, 363–371.
35. Myint, S.W.; Gober, P.; Brazel, A.; Grossman-Clarke, S.; Weng, Q. Per-pixel vs. object-based classification of urban land cover extraction using high spatial resolution imagery. *Remote Sens. Environ.* **2011**, *115*, 1145–1161. [[CrossRef](#)]
36. Tsai, F.; Chou, M.-J. Texture augmented analysis of high resolution satellite imagery in detecting invasive plant species. *J. Chin. Inst. Eng.* **2006**, *29*, 581–592. [[CrossRef](#)]
37. Haralick, R.M.; Shanmugam, K.; Dinstein, I. Textural Features for Image Classification. *IEEE Trans. Syst. Man Cybern.* **1973**, *SMC-3*, 610–621. [[CrossRef](#)]
38. Chen, D.; Stow, D.A.; Gong, P. Examining the effect of spatial resolution and texture window size on classification accuracy: An urban environment case. *Int. J. Remote Sens.* **2004**, *25*, 2177–2192. [[CrossRef](#)]
39. Franklin, S.E.; Hall, R.J.; Moskal, L.M.; Maudie, A.J.; Lavigne, M.B. Incorporating texture into classification of forest species composition from airborne multispectral images. *Int. J. Remote Sens.* **2000**, *21*, 61–79. [[CrossRef](#)]
40. Hall-Beyer, M. GLCM Texture Tutorial. Available online: <http://www.fp.ucalgary.ca/mhallbey/tutorial.htm> (accessed on 24 May 2017).
41. Mountrakis, G.; Im, J.; Ogole, C. Support vector machines in remote sensing: A review. *ISPRS J. Photogramm. Remote Sens.* **2011**, *66*, 247–259. [[CrossRef](#)]
42. Belgiu, M.; Drăguț, L. Random forest in remote sensing: A review of applications and future directions. *ISPRS J. Photogramm. Remote Sens.* **2016**, *114*, 24–31. [[CrossRef](#)]
43. Immitzer, M.; Atzberger, C.; Koukal, T. Tree Species Classification with Random Forest Using Very High Spatial Resolution 8-Band WorldView-2 Satellite Data. *Remote Sens.* **2012**, *4*, 2661–2693. [[CrossRef](#)]
44. Cortes, C.; Vapnik, V. Support-Vector Networks. *Mach. Learn.* **1995**, *20*, 273–297. [[CrossRef](#)]
45. Heumann, B.W. An Object-Based Classification of Mangroves Using a Hybrid Decision Tree—Support Vector Machine Approach. *Remote Sens.* **2011**, *3*, 2440–2460. [[CrossRef](#)]
46. Kavzoglu, T.; Colkesen, I. A kernel functions analysis for support vector machines for land cover classification. *Int. J. Appl. Earth Obs. Geoinf.* **2009**, *11*, 352–359. [[CrossRef](#)]
47. Liaw, A.; Wiener, M. Classification and regression by randomForest. *R News* **2002**, *2*, 18–22.

48. Meyer, D.; Dimitriadou, E.; Hornik, K.; Weingessel, A.; Leisch, F. *e1071: Misc Functions of the Department of Statistics, Probability Theory Group (Formerly: E1071), TU Wien*; [R Package e1071 Version 1.6-7]. Comprehensive R Archive Network (CRAN); 2017. Available online: <https://CRAN.R-project.org/package=e1071> (accessed on 1 March 2017).
49. Rodriguez, J.D.; Perez, A.; Lozano, J.A. Sensitivity Analysis of k-Fold Cross Validation in Prediction Error Estimation. *IEEE Trans. Pattern Anal. Mach. Intell.* **2010**, *32*, 569–575. [[CrossRef](#)] [[PubMed](#)]
50. Landis, J.R.; Koch, G.G. The measurement of observer agreement for categorical data. *Biometrics* **1977**, *33*, 159–174. [[CrossRef](#)] [[PubMed](#)]
51. Foody, G.M. Thematic map comparison: Evaluating the statistical significance of differences in classification accuracy. *Photogramm. Eng. Remote Sens.* **2004**, *70*, 627–633. [[CrossRef](#)]
52. Roberts, D.A.; Ustin, S.L.; Ogunjemiyo, S.; Greenberg, J.; Dobrowski, S.Z.; Chen, J.; Hinckley, T.M. Spectral and Structural Measures of Northwest Forest Vegetation at Leaf to Landscape Scales. *Ecosystems* **2004**, *7*, 545–562. [[CrossRef](#)]
53. Ng, W.-T.; Rima, P.; Einzmann, K.; Immitzer, M.; Atzberger, C.; Eckert, S. Assessing the Potential of Sentinel-2 and Pléiades Data for the Detection of *Prosopis* and *Vachellia* spp. in Kenya. *Remote Sens.* **2017**, *9*, 74. [[CrossRef](#)]
54. Pu, R.; Liu, D. Segmented canonical discriminant analysis of in situ hyperspectral data for identifying 13 urban tree species. *Int. J. Remote Sens.* **2011**, *32*, 2207–2226. [[CrossRef](#)]
55. Sheeren, D.; Fauvel, M.; Josipovic, V.; Lopes, M.; Planque, C.; Willm, J.; Dejoux, J.-F. Tree species classification in temperate forests using formosat-2 satellite image time series. *Remote Sens.* **2016**, *8*, 734. [[CrossRef](#)]
56. Eckert, S. Improved Forest Biomass and Carbon Estimations Using Texture Measures from WorldView-2 Satellite Data. *Remote Sens.* **2012**, *4*, 810–829. [[CrossRef](#)]
57. Pal, M. Random forest classifier for remote sensing classification. *Int. J. Remote Sens.* **2005**, *26*, 217–222. [[CrossRef](#)]
58. Czajka, C.; Braun, M.P.; Wink, M. Resource Use by Non-Native Ring-Necked Parakeets (*Psittacula krameri*) and Native Starlings (*Sturnus vulgaris*) in Central Europe. *Open Ornithol. J.* **2011**, *4*, 17–22. [[CrossRef](#)]
59. Wegener, S. Verbreitung und Arealnutzung der Halsbandsittiche (*Psittacula krameri*) in Heidelberg. *Ornithologische Gesellschaft Baden-Württemberg* **2007**, *23*, 39–55.
60. Clergeau, P.; Vergnes, A.; Delanoue, R. La perruche à collier *Psittacula krameri* introduite en Ile-de-France: Distribution et régime alimentaire. *Alauda* **2009**, *7*, 121–132.
61. Hernández-Brito, D.; Carrete, M.; Popa-Lisseanu, A.G.; Ibáñez, C.; Tella, J.L. Crowding in the City: Losing and Winning Competitors of an Invasive Bird. *PLoS ONE* **2014**, *9*, e100593. [[CrossRef](#)]
62. Franklin, S.E.; Wulder, M.A.; Gerylo, G.R. Texture analysis of IKONOS panchromatic data for Douglas-fir forest age class separability in British Columbia. *Int. J. Remote Sens.* **2001**, *22*, 2627–2632. [[CrossRef](#)]
63. He, K.S.; Bradley, B.A.; Cord, A.F.; Rocchini, D.; Tuanmu, M.-N.; Schmidtlein, S.; Turner, W.; Wegmann, M.; Pettorelli, N. Will remote sensing shape the next generation of species distribution models? *Remote Sens. Ecol. Conserv.* **2015**, *1*, 4–18. [[CrossRef](#)]

